COMMUNICATIONS IN COMPUTATIONAL PHYSICS
Vol. **2**, No. 1, pp. 73-86

Commun. Comput. Phys.
February 2007

Surface Diffusion on Stressed Solid Surface

Xiaofan Li[1,*] and Qing Nie[2]

[1] *Department of Applied Mathematics, Illinois Institute of Technology, Chicago, IL 60616, USA.*
[2] *Center for Mathematical and Computational Biology, Department of Mathematics, University of California, Irvine, CA 92697-3875, USA.*

Received 18 November 2005; Accepted (in revised version) 6 April 2006

Available online 30 August 2006

Abstract. The surface diffusion of an axi-symmetric solid, a whisker, subject to applied uniaxial stress, is studied numerically based on a new boundary integral formulation for periodic stress configurations. An efficient semi-implicit time-stepping scheme is developed to treat the serve stiffness due to high-order derivatives. When the initial perturbation is small the effect of the stress on the motion of the whisker is found to agree with the linear stability analysis. Numerical simulations of a fully nonlinear case are also presented, and a potential break-up of the whisker is observed.

Key words: Surface diffusion; elastic stress; boundary integral method; semi-implicit scheme.

1 Introduction

When a solid is heated, the atoms on the outer surface diffuse to form a thermodynamically lower energy configuration. Such a surface diffusion motion of a thin solid rod, a whisker, driven by surface energy only, was first studied by Nichols and Mullins (1965) [8]. They derive the Rayleigh criteria for stability of a cylinder, i.e., it is unstable to axi-symmetric perturbations whose wavelength exceeds the circumference of the unperturbed cylinder. This result is analogous to the classical Rayleigh instability of a cylinder of a fluid under surface tension. In both cases, the instability causes the cylinder to pinchoff forming a chain of spheres that minimizes the surface energy for a fixed volume. Through second- and higher-order perturbation arguments and finite-element calculations, Coleman *et al.* [2, 3] have shown that a cylinder is unstable to perturbations of certain combination of linearly

*Correspondence to: Xiaofan Li, Department of Applied Mathematics, Illinois Institute of Technology, Chicago, IL 60616, USA. Email: lix@iit.edu

stable wavelengths. The surface diffusion and the self-similar axi-symmetric pinchoff of a cylinder have been examined using asymptotic, numerical and analytical methods by several authors. For a review and the references, see Bernoff *et al.* [1].

The effect of elastic stress on the morphological instability of a whisker has been studied by linear stability analysis in Colin *et al.* (1997) [4] and Kirill *et al.* (1998) [6]. The results show that short-wavelength instability can develop when the applied stress is beyond a critical value and non-axisymmetric modes can be excited under certain conditions.

In this work, we investigate the fully nonlinear evolution of an axi-symmetric whisker when the stress is present. In Section 2, we state the problem in which the whisker is periodic in one direction and subject to a periodic applied stress. In Section 3, two equivalent boundary integral formulations of the problem are derived, enabling the sharp-interface numerical simulation.

The nonlinear evolution equation for the whisker involves surface diffusion of the interface curvature. This fourth-order derivative term puts a severe constraint on the time-step when explicit temporal schemes are used. On the other hand, any fully implicit schemes require solving nonlinear systems at every time-step, and it is extremely expensive. In this paper, we present an efficient semi-implicit temporal scheme for interfaces in axi-symmetric geometry based on the local decomposition technique [9, 11, 15]. Realizing that the meridian term in the mean curvature for an axi-symmetric interface dominates the stability property of a temporal scheme, we express it in terms of the tangent angle of the interface. As a result, the most stiff term reduces to a fourth-order derivative of the tangent angle, and it becomes linear in Fourier space. We treat this term implicitly and the rest of the nonlinear terms in low-oder derivative explicitly. A detailed description of the numerical methods is presented in Section 4. In Section 5, our formulation of the problem and numerical methods are validated using the results from linear stability analysis and the effect of elastic stress is investigated in nonlinear evolution region.

2 Governing equations

Consider an infinite cylinder, periodic on the x-direction with period L_p, as shown in Fig. 1. Denote the cylinder by Ω, its boundary/surface by $\partial\Omega$, and its outward unit normal by $\mathbf{n}$. Let $\partial\Omega_l$ be a cross section of the cylinder with a plane perpendicular to x-axis, and $\partial\Omega_r$ be the first periodic image of $\partial\Omega_l$ to the right. $\partial\Omega_p$ is the one-period section of cylinder surface that is between $\partial\Omega_l$ and $\partial\Omega_r$.

The surface of the cylinder evolves due to surface diffusion which minimizes the sum of the surface energy and elastic energy. Its normal velocity is given by ([6] and references therein)

$$v_n = \frac{\partial \mathbf{x}}{\partial t} \cdot \mathbf{n} = \nabla_s^2(\beta g^{el} - \kappa), \tag{2.1}$$

where $\kappa = \boldsymbol{\nabla} \cdot \mathbf{n}$ is the sum of the principle curvatures, g^{el} is the elastic energy density, and the dimensionless parameter β measures the relative magnitude of the elastic energy compared with the surface energy. Both g^{el} and β will be defined later.

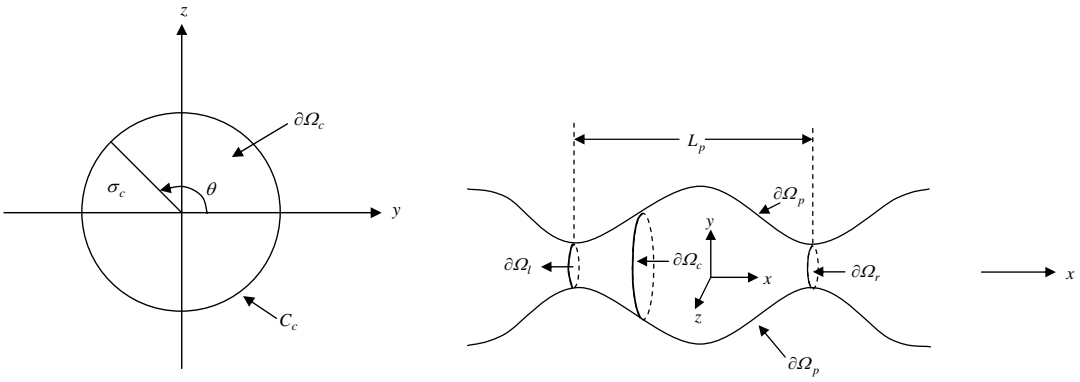

Figure 1: Sketch of a periodic whisker.

The presence of the elastic effects arises due to applied stresses in the solid. Next we describe the governing equations for obtaining the elastic energy. The solid is at mechanical equilibrium in absence of body forces,

$$\boldsymbol{\nabla} \cdot \boldsymbol{\sigma} = \mathbf{0}, \qquad \text{for } \mathbf{x} \text{ in } \Omega, \tag{2.2}$$

where $\boldsymbol{\sigma}$ denotes the stress tensor. Since outside the solid is vacuum, the surface of the cylinder is a traction-free surface,

$$\mathbf{t} \equiv \boldsymbol{\sigma} \cdot \mathbf{n} = \mathbf{0}, \qquad \text{for } \mathbf{x} \text{ on } \partial\Omega. \tag{2.3}$$

The relation between the stress and strain tensors follows Hooke's law for isotropic elasticity, i.e. $\sigma_{ij} = 2\mu\epsilon_{ij} + \lambda\epsilon_{kk}\delta_{ij}$, where μ and λ are the Lamé constants. Stress in the solid arises due to an applied stress in the solid. The stress is applied such that

$$\int_{\partial\Omega_r} \mathbf{t} \, \mathrm{d}A = \mathbf{F}, \tag{2.4}$$

where $\mathbf{F}$ is a constant vector and the normal to $\partial\Omega_r$ is the unit vector along x-axis $\mathbf{e}_1 = (1, 0, 0)$. It is important to note that the condition (2.4) is actually satisfied at any cross section of the cylinder because of Eqs. (2.2) and (2.3) and the divergence theorem. The elasticity problem is complete by adding the periodic boundary conditions

$$\mathbf{u}(\mathbf{x} + L_p\mathbf{e}_1) - \mathbf{u}(\mathbf{x}) = \mathbf{U}, \quad \mathbf{t}(\mathbf{x} + L_p\mathbf{e}_1) + \mathbf{t}(\mathbf{x}) = \mathbf{0}, \tag{2.5}$$

for any $\mathbf{x}$ in the solid. Note the normal vectors in the second equation of (2.5) are in opposite directions at $\mathbf{x}$ and its periodic image $\mathbf{x} + L_p\mathbf{e}_1$. In this work, we specify a constant vector $\mathbf{U} = (U_1, 0, 0)$. For the axi-symmetric case, it is clear that $F_2 = F_3 = 0$ where (F_1, F_2, F_3) is the Cartesian coordinates of $\mathbf{F}$. Also, it can be shown (see Appendix) that the first component of U_1 is related to F_1 through the following integral equation

$$L_pF_1 = (2\mu + \lambda)\left[\pi\sigma_r^2 U_1 - 2\pi\int_C u_1\sigma \, \mathrm{d}\sigma\right] + 2\pi\lambda\int_C u_\sigma\sigma \, \mathrm{d}x, \tag{2.6}$$

where σ_r is the radius of the disk $\partial\Omega_r$, $\mathbf{u} = (u_1, u_\sigma, 0)$ in the cylindrical coordinates (x, σ, ϕ), C is the oriented contour of the surface $\partial\Omega_p$ in $(x.y)$-plane in the direction of increasing x, $\sigma = y$ is the distance of C to x-axis.

Given $\mathbf{U}$ or $\mathbf{F}$, the displacement $\mathbf{u}$ and the traction $\mathbf{t}$ on $\partial\Omega$ can be obtained by solving the equations (2.2)–(2.6). Then, the elastic energy density $g^{el} = \frac{1}{2}\boldsymbol{\sigma} \cdot \boldsymbol{\epsilon}$ can be computed through a local coordinate transformation [5, 13].

3 Boundary integral formulation

Suppose V is a finite volume of the solid enclosed by the surface S. For a point $\mathbf{x}$ on S,

$$\iint_S [u_i(\mathbf{y}) - u_i(\mathbf{x})] T_{ijk}(\mathbf{y} - \mathbf{x}) n_k(\mathbf{y}) \, \mathrm{d}A_{\mathbf{y}} = \iint_S t_i(\mathbf{y}) G_{ij}(\mathbf{y} - \mathbf{x}) \, \mathrm{d}A_{\mathbf{y}}, \tag{3.1}$$

where $j = 1, 2, 3$. Here, G_{ij} and T_{ijk} are the Green's functions associated with the displacement and stress, respectively. Einstein summation notation is used in this work. Note the integrands in Eq. (3.1) are weakly singular and there are no principal value integrals.

If V is one period of the solid Ω, restricting our attention to a system that is L_p-periodic in x-axis and applying the boundary conditions Eqs. (2.3) and (2.5), we obtain from Eq. (3.1)

$$\iint_{\partial\Omega_p} [u_i(\mathbf{y}) - u_i(\mathbf{x})] T^P_{ijk}(\mathbf{y} - \mathbf{x}) n_k(\mathbf{y}) \, \mathrm{d}A_{\mathbf{y}} = -U_i \iint_{\partial\Omega_r} T^P_{ijk}(\mathbf{y} - \mathbf{x}) n_k(\mathbf{y}) \, \mathrm{d}A_{\mathbf{y}}, \tag{3.2}$$

where T^P_{ijk} are the corresponding Green's functions that are L_p-periodic on the x-direction.

Alternatively, we can decompose the stress field $(\boldsymbol{\sigma}, \mathbf{u})$ into a uniaxial stress, $\boldsymbol{\sigma}^{(0)} = \mathrm{diag}(1, 0, 0)$ and $\mathbf{u}^{(0)} = (x, -\nu y, -\nu z)$, and the disturbance field, $(\boldsymbol{\sigma}^D, \mathbf{u}^D)$ for a point $\mathbf{x} = (x, y, z)$ in Cartesian coordinates.

We specify $\mathbf{u}^{(0)}$ according to Eqs. (2.6) such that the disturbance fields $\mathbf{u}^D \equiv \mathbf{u} - \mathbf{u}^{(0)}$ and $\mathbf{t}^D \equiv \mathbf{t} - \mathbf{t}^{(0)}$ are L_p-periodic on the x-direction.

Applying Eq. (3.1) to $(\mathbf{u}^D, \mathbf{t}^D)$ for one period of the solid, we obtain

$$\iint_{\partial\Omega_p} [u^D_i(\mathbf{y}) - u^D_i(\mathbf{x})] T^P_{ijk}(\mathbf{y} - \mathbf{x}) n_k(\mathbf{y}) \, \mathrm{d}A_{\mathbf{y}} = -\iint_{\partial\Omega_p} t^{(0)}_i(\mathbf{y}) G^P_{ij}(\mathbf{y} - \mathbf{x}) \, \mathrm{d}A_{\mathbf{y}}. \tag{3.3}$$

It can be shown that Eqs. (3.2) and (3.3) are equivalent.

When $\mathbf{F} = F_1 \mathbf{e}_1$, we have

$$\begin{aligned} \mathbf{u}^{(0)} &= \frac{U_1}{L_p}(x\mathbf{e}_1 - \nu y \mathbf{e}_2 - \nu z \mathbf{e}_3) = \frac{U_1}{L_p}(x\mathbf{e}_1 - \nu\sigma\hat{\boldsymbol{\sigma}}) \\ \mathbf{t}^{(0)} &\equiv \boldsymbol{\sigma}^{(0)} \cdot \mathbf{n} = \frac{U_1}{L_p}\mathrm{diag}(E, 0, 0) \cdot \mathbf{n} = \frac{U_1 E n_1}{L_p}\mathbf{e}_1, \end{aligned} \tag{3.4}$$

where $\hat{\boldsymbol{\sigma}}$ denotes the unit vector in σ-direction of the cylindrical coordinates (x, σ, ϕ), $E = 2\mu(1+\nu)$ is the Young's modulus and n_1 is the x-component of the outward unit vector $\mathbf{n}$ normal to C. The value of U_1 is related to F_1 according to Eq. (2.6), or equivalently (see Appendix)

$$L_p F_1 = \frac{U_1}{L_p} E V_p - 2\pi(2\mu + \lambda) \int_C u_1^D \sigma \, \mathrm{d}\sigma + 2\pi\lambda \int_C u_\sigma^D \sigma \, \mathrm{d}x, \tag{3.5}$$

where V_p is the volume of the solid in one period Ω_p.

4 Numerical methods

The motion of interface C, $x(\alpha, t)\mathbf{e}_1 + \sigma(\alpha, t)\hat{\boldsymbol{\sigma}}$, can be reposed in terms of its local arclength derivatives s_α and its tangent angle θ defined implicitly from the definition of the tangent vector,

$$\mathbf{s}(\alpha, t) = (x_\alpha, \sigma_\alpha)/s_\alpha = (\sin\theta(\alpha, t), \cos\theta(\alpha, t)). \tag{4.1}$$

Then θ and s_α satisfy

$$s_{\alpha t} = T_\alpha + \theta_\alpha v_n, \tag{4.2}$$

$$\theta_t = -\frac{v_{n\alpha} + T\theta_\alpha}{s_\alpha}, \tag{4.3}$$

where $\mathbf{s}$ is the tangential direction of the interface with T as a specified tangential velocity. Notice that the choice of T does not affect the motion of the interface C, and it only affects the definition of α. In particular, the tangential velocity,

$$T(\alpha, t) = -\frac{\alpha}{2\pi} \int_0^{2\pi} \theta_{\alpha'} v_n \mathrm{d}\alpha' + \int_0^{\alpha} \theta_{\alpha'} v_n \mathrm{d}\alpha', \tag{4.4}$$

leads to a constant s_α in space satisfying

$$\frac{L(t)}{2\pi} \equiv s_\alpha(\alpha, t), \tag{4.5}$$

where L is the length of C. Accordingly, the equation (4.2) for s_α becomes

$$L_t = -\int_0^{2\pi} \theta_{\alpha'} v_n \mathrm{d}\alpha'. \tag{4.6}$$

The curvature κ can be decompose into

$$\kappa \equiv \kappa_{2d} + \kappa_\infty, \tag{4.7}$$

where κ_{2d} and κ_∞ are the curvatures in the meridian and azimuthal directions respectively:

$$\kappa_{2d} = \frac{\sigma_\alpha x_{\alpha\alpha} - \sigma_{\alpha\alpha} x_\alpha}{s_\alpha^3} = \theta_s, \qquad \kappa_\infty = \frac{x_\alpha}{\sigma s_\alpha}. \tag{4.8}$$

In an axi-symmetric geometry, the surface Laplacian reduces to

$$\boldsymbol{\nabla}_s^2 = \frac{\partial^2}{\partial s^2} + \frac{\sigma_s}{\sigma}\frac{\partial}{\partial s}. \tag{4.9}$$

Thus the evolution equation (2.1) becomes

$$v_n = -\theta_{sss} + P, \tag{4.10}$$

where

$$P = -\frac{\sigma_s}{\sigma}\frac{\partial \kappa_{2d}}{\partial s} + \boldsymbol{\nabla}_s^2(-\kappa_\infty + \beta g^{el}). \tag{4.11}$$

Similar to the numerical method for axi-symmetric vortex sheets [9], the evolution equation for θ is decomposed locally with one term involving the fourth order of derivative and the rest of terms only involving low order derivatives:

$$\theta_t = -\theta_{ssss} + (P_s + T\theta_s). \tag{4.12}$$

The equation for the corresponding Fourier coefficients of θ becomes

$$\hat{\theta}_t = -\left(\frac{2\pi}{L}\right)^4 k^4\hat{\theta}(k) + \hat{A}(k), \tag{4.13}$$

where $\hat{A}(k)$ is the Fourier coefficient for $P_s + T\theta_s$.

Because the temporal stability constraint is dictated by the term with the highest order of derivative, a standard explicit scheme, such as a Runge-Kutta or a linear multi-step type of method, applied to Eq. (4.13) requires a time-step proportional to the inverse of k^4. On the other hand, a fully implicit temporal scheme on Eq. (4.13) leads to nonlinear systems that have to be solved at every time-step. For both approaches, the computational costs are very expensive, and become prohibitive for medium to large spatial resolutions.

Realizing that the fourth-order derivative term is linear (and diagonalized in Fourier space) and decoupled from the terms with lower order derivatives in Eq. (4.13), one can treat the $k^4\hat{\theta}(k)$ term implicitly and the nonlinear term explicitly such that the stability constraint associated with the fourth-order derivative term is removed without the need of solving any nonlinear systems.

In particular, one can apply the Crank-Nicholson discretization on the linear term and the leapfrog method on the nonlinearity in Eq. (4.13) to obtain

$$\frac{\hat{\theta}^{n+1}(k) - \hat{\theta}^{n-1}(k)}{2\triangle t} = -k^4\left[\left(\frac{2\pi}{L^{n+1}}\right)^4\hat{\theta}^{n+1}(k) + \left(\frac{2\pi}{L^{n-1}}\right)^4\hat{\theta}^{n-1}(k)\right] + \hat{A}(k). \tag{4.14}$$

This equation can be easily solved explicitly for θ^{n+1}. Similar approaches have been successfully applied for two-dimensional vortex sheets and Hele-shaw flows [10, 15] as well as for axisymmetric vortex sheets [9]. In addition, Eq. (4.13) can also be approximated

using the integration factor methods [15] and modified integration factor methods [7] that have advantages of damping small-scale numerical oscillations to make simulations more robust and stable.

In order to evaluate the elastic energy density g^{el} in Eq. (4.13) at each time step, we must solve the boundary integral equations for the elasticity, either Eq. (3.2) or Eq. (3.3). The weakly singular integrals in the equations are partially de-singularized through the identities. A collocation method is carried out for the integral equations in which the integrals are approximated by the composite six-point Guassian quadratures. The quadrature points are obtained via the quintic spline interpolation of the equally spaced nodes representing the interface. The FFT is used to calculate the derivatives of various quantities and the pseudo-spectral method is applied for the nonlinear terms (e.g. P). The discretized equations for the displacement and the traction at the nodes are solved using GMRES [12]. Once the displacement and traction are obtained, the elastic energy density g^{el} can be computed as in [5, 13].

5 Results

The dynamics of the whisker depends on the dimensionless parameter $\beta \equiv R_0 E\tilde{\epsilon}^2/\gamma$. This parameter measures the relative strength of the elastic energy compared with the surface energy. Here, R_0 is the radius of the undisturbed cylinder used as the length scale, E is Young's modulus, $\tilde{\epsilon} = U_1/R_0$ is the scale of the applied strain, and γ is the solid-vapour surface tension. The corresponding time scale is chosen as $R_0^4 k_T/(D_s\gamma V_a^2 A_0)$, where D_s is the surface diffusivity coefficient, V_a is the atomic volume, A_0 is the number of atoms per unit area on the interface, and k_T is the thermal energy.

To validate the numerical implementation, we test an exact solution of the straight cylinder for the elasticity equations (3.2). It is found that the numerical calculation of the integrals involving the x-component is usually more accurate than those involving the σ-component. This is mainly due to the nature of singularity of the integrands in the σ-components. It is also observed that the numerical solutions from solving Eq. (3.3) are more accurate than the ones from Eq. (3.2) when the disturbance field is relatively small compared with the applied stress field. The difference is owing to the fact that the numbers of significant digits in the solutions of Eqs. (3.2) and (3.3) are the same but Eq. (3.2) solves for the total field $\mathbf{u}$ while Eq. (3.3) solves for the disturbance field $\mathbf{u}^D$ that can be treated as a small correction term to the principal term $\mathbf{u}^{(0)}$. For the rest of the paper, the elasticity energy density g^{el} is computed based on the numerical solutions of Eq. (3.3).

Next, we compare our numerical simulation with the result of linear analysis [4, 6]. The applied stress on the whisker given by the condition (2.4) of this paper agree with that in the linear studies up to the leading order. We show that our results match well with the prediction in [4, 6] for small-wavenumber disturbance. Fig. 2 displays the shape evolution of a slightly disturbed circular cylinder, $\sigma = 1 + 0.001\cos(2k\pi x)$ for the wavenumber

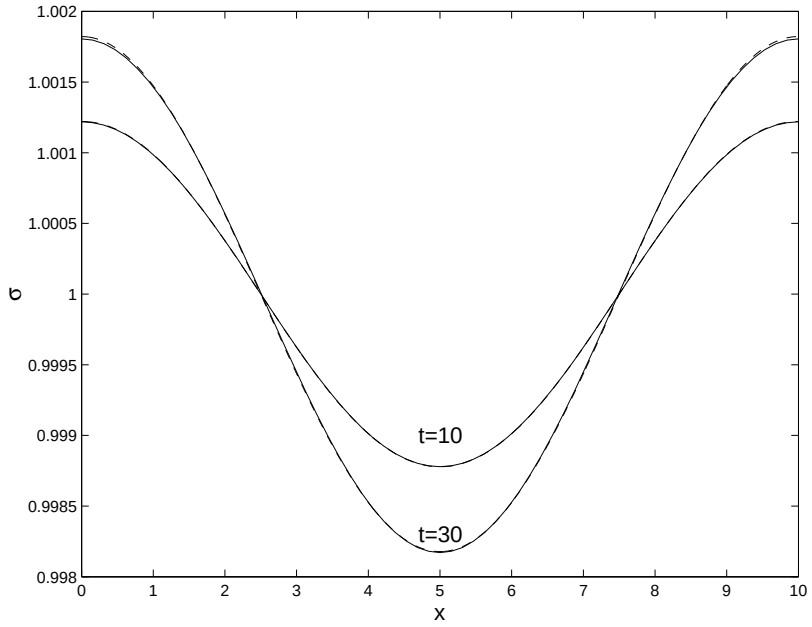

Figure 2: Comparison with the linear analysis in [4, 6] for a cylindrical whisker with the initial profile $\sigma = 1 + 0.001\cos(2k\pi x)$ and the wavenumber $k = 0.1$. The contours of the whisker are shown at the nondimensionalized time $t = 10$ and 30, where the solid and dashed lines are obtained from the numerical simulation and the linear stability analysis respectively.

$k = 0.1$, the elastic parameter $\beta = 1/2$ and the Poisson ratio $\nu = 1/3$. The solid lines in Fig. 2 are obtained from our numerical simulation while the dashed lines correspond to the linear solution $\sigma = 1 + 0.001\exp(\omega t)\cos(2k\pi x)$ where the growth rate is the small-k asymptotic result $\omega \sim (1 + 2\beta)k^2 + \mathcal{O}(k^4)$ given in [6].

We turn to investigate the effect of elasticity on the evolution of a cylindrical whisker where the initial shape significantly away from a straight cylinder. The initial whisker profile is given by $\sigma = 1 + 0.1\cos(2k\pi x)$ with the wavenumber $k = 1.2$.

Fig. 3 shows a time series of the whisker profiles for $\nu = 1/3$ and $\beta = 1/8$. It is clear that the whisker evolves to a straight circular cylinder agreeing with the linear analysis that predicts stability at these values of wavenumber and the elastic parameter. In order to show the accuracy of the computation, we have shown the numerical results of two different discretizations: the solid lines are for the number of marker points $n = 128$ while the dashed lines in the figure are for $n = 64$. The results are indistinguishable in the plot, demonstrating that the resolution with $n = 64$ is enough for the case. Thus, in this paper, we have obtained the results starting with $n = 64$.

When β is raised to 1/4, the whisker becomes unstable based on the linear analysis. Fig. 4 shows the snap shots of the whisker profiles at times $t = 2/1.2^4, 3.6/1.2^4, 3.98/1.2^4$. The numerical results show that the whisker pinches at the narrow sections and the dynamics accelerates as the whisker collapses. Further detail at the pinching portions are

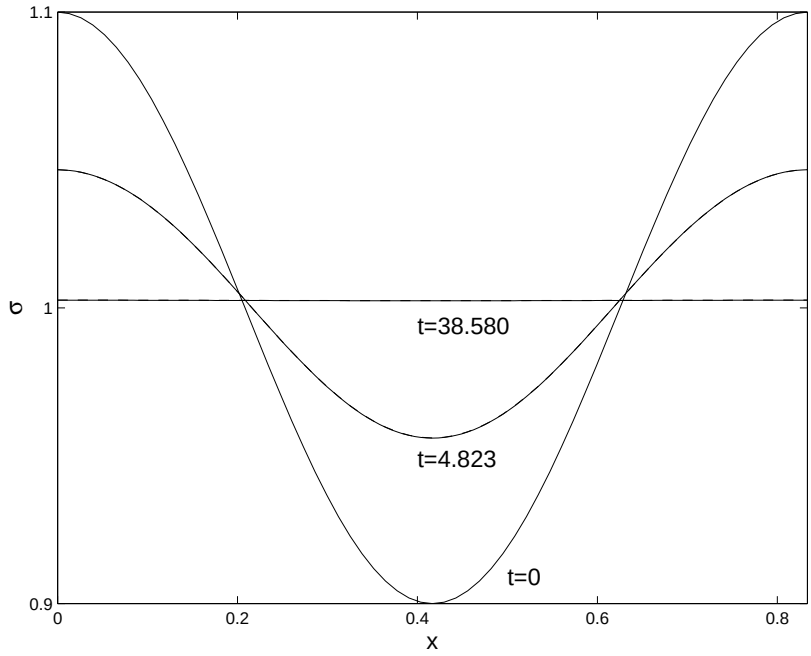

Figure 3: Evolution of a cylindrical whisker with the initial profile $\sigma = 1 + 0.1\cos(2k\pi x)$ with the wavenumber $k = 1.2$ and $\beta = 1/8$. The cross sections in the (x, y)-plane of the whisker are shown at the nondimensionalized time $t = 10/1.2^4 \approx 4.823$ and $t = 80/1.2^4 \approx 38.580$. The figure shows both the results obtained with the number of marker points $n = 64$ (the dashed lines) and with $n = 128$ (the solid lines).

under current study.

5.1 Conclusions

In this work, we have developed a model such that the effect of elastic stress on surface diffusion can be investigated numerically for an axi-symmetric, periodic whisker. In particular, the applied stress must satisfy the relationship (2.6) between the traction and the displacement in the solid, and the displacement vector must have a jump between two periodic boundaries for a stressed solid in the periodic configuration.

To facilitate numerical simulation using sharp-interface methods, we have derived the boundary integral equations for the elasticity problem using the three-dimensional, axi-symmetric Green's functions. The boundary integral approach reduces the original three-dimensional problem to a two-dimensional one, and, further, restricting to axi-symmetry makes it a one-dimensional computation in which the details of the dynamics can be obtained accurately. To deal with the stiffness associated with the surface diffusion on the curvature, we have developed an efficient semi-implicit temporal scheme for the interface motion in axi-symmetric geometry. In the new scheme, the most stiff term reformulated in Fourier space becomes a diagonal system, thus an implicate treatment can be easily implemented without extra costs. This new temporal scheme allows us perform long-time

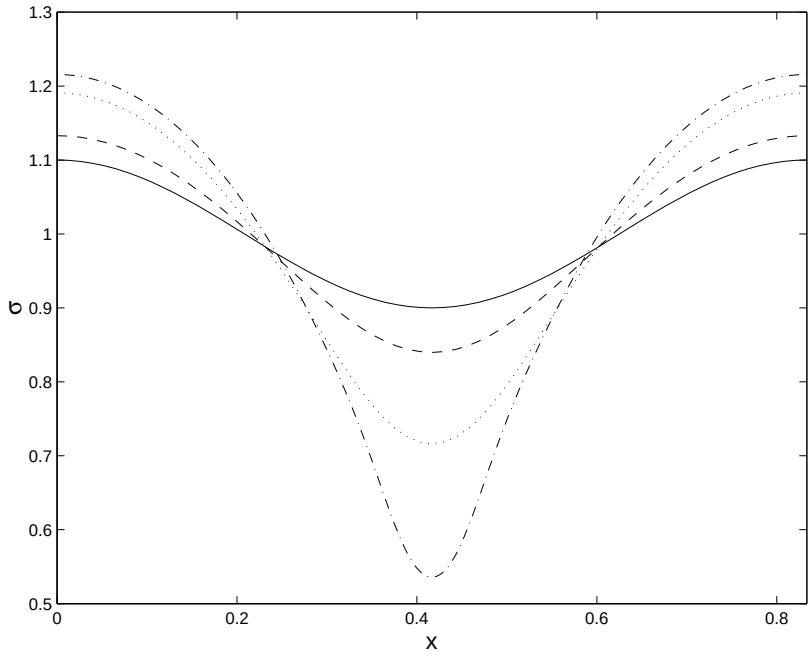

Figure 4: Evolution of a cylindrical whisker with the initial profile $\sigma = 1 + 0.1\cos(2k\pi x)$ with the wavenumber $k = 1.2$ (shown by the solid line) and $\beta = 1/4$. The cross sections in the (x, y)-plane of the whisker are shown at the nondimensionalized time $t = 2/1.2^4 \approx 0.965$ (the dashed line), $3.6/1.2^4 \approx 1.736$ (the dotted line), and $3.98/1.2^4 \approx 1.919$ (the dash-dotted line).

and robust simulations to examine the effect of elasticity.

We have performed simulations of fully nonlinear evolution of a whisker under influence of applied stress. Our results agree well with the linear stability analysis when the initial perturbation from the equilibrium shape is small. We also have presented the whisker profiles at different times for a linearly unstable configuration.

In absence of stress, an axi-symmetric whisker may pinch off in finite time, minimizing its surface energy. Further, it has been shown that the pinch-off structure is self-similar and there is a unique observable cone angle during pinch-off. [1] In contrast, in two-dimensional studies, solid surfaces form cusps under applied stress. [14, 16] It would be interesting to examine whether an axi-symmetric whisker pinches off first or develop a surface singularity first, under stress. The dynamics of this kind is under current investigation.

Acknowledgments

The authors would like thank M. J. Miksis for first introducing the problem to us. The work was partially supported by NSF DMS-0511411 (X.L.) and NSF DMS-0511169 (Q.N.).

A Derivation of Eqs. (2.6) and (3.5)

The Cartesian coordinates is used unless where it is specified otherwise. As shown earlier, for any cross section $\partial\Omega_c$ of the cylindrical solid with normal $\mathbf{n} = (1, 0, 0)$,

$$F_i = \iint_{\partial\Omega_c} t_i \mathrm{d}A = \iint_{\partial\Omega_c} \sigma_{ij} n_j \mathrm{d}A = \iint_{\partial\Omega_c} \sigma_{i1} \mathrm{d}A. \tag{A.1}$$

For isotropic elasticity, the Hooke's law gives

$$\sigma_{i1} = 2\mu\epsilon_{i1} + \lambda\delta_{i1}\epsilon_{kk},$$

or

$$\begin{aligned} \sigma_{11} &= (2\mu + \lambda)u_{1,1} + \lambda(u_{2,2} + u_{3,3}), \\ \sigma_{i1} &= \mu(u_{i,1} + u_{1,i}), \quad i = 2, 3. \end{aligned} \tag{A.2}$$

Using Green's Theorem and the axi-symmetry, we have

$$\begin{aligned} \iint_{\partial\Omega_c} u_{1,2} \mathrm{d}A &= \int_{C_c} u_1 \mathrm{d}z = u_1 \int_{C_c} \mathrm{d}z = 0 \\ \iint_{\partial\Omega_c} u_{1,3} \mathrm{d}A &= -\int_{C_c} u_1 \mathrm{d}y = -u_1 \int_{C_c} \mathrm{d}y = 0, \end{aligned} \tag{A.3}$$

where C_c is the boundary of $\partial\Omega_c$.

Express C_c by the parametric equations $y = \sigma_c \cos\theta, z = \sigma_c \sin\theta$ where σ_c is the radius of the circular disk $\partial\Omega_c$, and write the displacement $\mathbf{u} = u_1\mathbf{e}_1 + u_\sigma\hat{\boldsymbol{\sigma}}$ (in cylindrical coordinates, $\hat{\boldsymbol{\sigma}}$ is the unit vector in σ-direction) as $\mathbf{u} = u_1\mathbf{e}_1 + u_\sigma \cos\theta\mathbf{e}_2 + u_\sigma \sin\theta\mathbf{e}_3$. Using Green's Theorem and calculating the line integrals, we obtain

$$\begin{aligned} \iint_{\partial\Omega_c} u_{2,2} \mathrm{d}A &= \int_{C_c} u_2 \mathrm{d}z = \pi\sigma_c u_\sigma \\ \iint_{\partial\Omega_c} u_{3,3} \mathrm{d}A &= -\int_{C_c} u_3 \mathrm{d}y = \pi\sigma_c u_\sigma. \end{aligned} \tag{A.4}$$

Using the Hooke's law (A.2),

$$\begin{aligned} F_1 &= \iint_{\partial\Omega_c} \sigma_{11} \mathrm{d}A = \iint_{\partial\Omega_c} \left[(2\mu + \lambda)u_{1,1} + \lambda(u_{2,2} + u_{3,3})\right] \mathrm{d}A \\ &= (2\mu + \lambda) \iint_{\partial\Omega_c} (u_{1,1} + u_{2,2} + u_{3,3}) \mathrm{d}A - 2\mu \iint_{\partial\Omega_c} (u_{2,2} + u_{3,3}) \mathrm{d}A. \end{aligned} \tag{A.5}$$

Integrate (A.5) over one period of the solid, and use the divergence theorem and Eq. (A.4), to derive

$$\begin{aligned} L_pF_1 =&(2\mu+\lambda)\iiint_{\Omega^P}(u_{1,1}+u_{2,2}+u_{3,3})\mathrm{d}V-4\pi\mu\int_C u_\sigma\sigma\mathrm{d}x,\\ L_pF_1 =&(2\mu+\lambda)\iint_{\partial\Omega_l+\partial\Omega_r+\partial\Omega_p}\mathbf{u}\cdot\mathbf{n}\mathrm{d}A-4\pi\mu\int_C u_\sigma\sigma\mathrm{d}x. \end{aligned} \tag{A.6}$$

Using the condition (2.5), we get

$$\begin{aligned} L_pF_1 =&(2\mu+\lambda)\iint_{\partial\Omega_r}(\mathbf{u}(\mathbf{x})-\mathbf{u}(\mathbf{x}-L_p\mathbf{e}_1))\cdot\mathbf{n}\mathrm{d}A\\ &+(2\mu+\lambda)\iint_{\partial\Omega_p}\mathbf{u}\cdot\mathbf{n}\mathrm{d}A-4\pi\mu\int_C u_\sigma\sigma\mathrm{d}x,\\ L_pF_1 =&(2\mu+\lambda)U_1\pi\sigma_r^2+(2\mu+\lambda)\iint_{\partial\Omega_p}\mathbf{u}\cdot\mathbf{n}\mathrm{d}A-4\pi\mu\int_C u_\sigma\sigma\mathrm{d}x. \end{aligned} \tag{A.7}$$

To simplify, we compute $\mathbf{u}\cdot\mathbf{n}$ on the contour C,

$$\mathbf{u}=u_1\mathbf{e}_1+u_\sigma\mathbf{e}_2,\qquad \mathbf{n}=-\frac{\mathrm{d}y}{\mathrm{d}s}\mathbf{e}_1+\frac{\mathrm{d}x}{\mathrm{d}s}\mathbf{e}_2. \tag{A.8}$$

Due to axi-symmetry and $\mathrm{d}A=\sigma\,\mathrm{d}\phi\,\mathrm{d}s$, where s is the arclength along C, we have

$$\iint_{\partial\Omega_p}\mathbf{u}\cdot\mathbf{n}\,\mathrm{d}A=2\pi\int_C(-u_1\sigma\,\mathrm{d}y+u_\sigma\sigma\,\mathrm{d}x). \tag{A.9}$$

Thus, Eq. (A.7) can be simplified to

$$L_pF_1=(2\mu+\lambda)\left[\pi\sigma_r^2U_1-2\pi\int_C u_1\sigma\,\mathrm{d}y+2\pi\int_C u_\sigma\sigma\,\mathrm{d}x\right]-4\pi\mu\int_C u_\sigma\sigma\,\mathrm{d}x, \tag{A.10}$$

which is the formula (2.6).

To obtain the formula (3.5), decompose $\mathbf{u}=\mathbf{u}^D+\mathbf{u}^{(0)}$ and note the periodic $\mathbf{u}^D$ and plug into the first equation of (A.6), using the definitions (3.4)

$$\begin{aligned} L_pF_1 &= (2\mu+\lambda)\iiint_{\Omega^P}(\boldsymbol{\nabla}\cdot\mathbf{u}^D+\boldsymbol{\nabla}\cdot\mathbf{u}^{(0)})\mathrm{d}V-4\pi\mu\int_C(u_\sigma^D+u_\sigma^{(0)})\sigma\mathrm{d}x\\ &= (2\mu+\lambda)\frac{U_1}{L_p}(1-2\nu)V_p+(2\mu+\lambda)\iint_{\partial\Omega_l+\partial\Omega_r+\partial\Omega_p}\mathbf{u}^D\cdot\mathbf{n}\mathrm{d}A\\ &\quad -4\pi\mu\int_C\frac{U_1}{L_p}(-\nu\sigma^2)\mathrm{d}x-4\pi\mu\int_C u_\sigma^D\sigma\mathrm{d}x \end{aligned} \tag{A.11}$$

Using the definition $\lambda = 2\mu\nu/(1-2\nu)$ and the periodicity of $\mathbf{u}^D$, we can simplify (A.11) to

$$L_pF_1 = \frac{U_1}{L_p}2\mu(1-\nu)V_p + (2\mu+\lambda)\iint\limits_{\partial\Omega_p}\mathbf{u}^D\cdot\mathbf{n}\mathrm{d}A + \frac{U_1}{L_p}4\mu\nu\int_C\pi\sigma^2\mathrm{d}x - 4\pi\mu\int_C u_\sigma^D\sigma\mathrm{d}x.$$

By the definition of V_p, we have

$$L_pF_1 = \frac{U_1}{L_p}2\mu(1-\nu)V_p + (2\mu+\lambda)\iint\limits_{\partial\Omega_p}\mathbf{u}^D\cdot\mathbf{n}\mathrm{d}A + \frac{U_1}{L_p}4\mu\nu V_p - 4\pi\mu\int_C u_\sigma^D\sigma\mathrm{d}x, \quad \text{(A.12)}$$

which gives

$$L_pF_1 = \frac{U_1}{L_p}EV_p + (2\mu+\lambda)\iint\limits_{\partial\Omega_p}\mathbf{u}^D\cdot\mathbf{n}\mathrm{d}A - 4\pi\mu\int_C u_\sigma^D\sigma\,\mathrm{d}x. \quad \text{(A.13)}$$

Similar to the simplification procedure from Eq. (A.7) to (2.6), Eq. (A.12) can be reduced to (3.5).

References

[1] A. J. Bernoff, A. L. Bertozzi and T. P. Witeleski, Axisymmetric surface diffusion: Dynamics and stability of self-similar pinchoff, J. Stat. Phys., 93 (1998), 725–776.

[2] B. D. Coleman, R. S. Falk and M. Moakher, Stability of cylindrical bodies in the theory of surface diffusion, Physica D, 89 (1995), 123–135.

[3] B. D. Coleman, R. S. Falk and M. Moakher, Space-time finite element methods for surface diffusion with applications to the theory of the stability of cylinders, SIAM J. Sci. Comput., 17 (1996), 1434–1448.

[4] J. Colin, J. Grilhè and N. Junqua, Surface instabilities of a stressed cylinderical whisker, Philos. Mag. A, 76 (1997), 793–805.

[5] H. J. Jou, P. H. Leo and J. S. Lowengrub, Microstructural evolution in inhomogeneous elastic media, J. Comput. Phys., 131 (1997), 109–148.

[6] D. J. Kirill, S. H. Davis, M. J. Miksis and P. W. Voorhees, Morphological instability of a whisker, Proc. R. Soc. A, 455 (1999), 3825–3844.

[7] P. H. Leo, J. S. Lowengrub and Q. Nie, Microstructural evolution in orthotropic elastic media, J. Comput. Phys., 157 (2000), 44–88.

[8] F. A. Nichols and W. W. Mullins, Surface- (interface-) and volume-diffusion contributions to morphological changes driven by capillarity, Trans. Metal. Sco. AIME, 233 (1965), 1840–1848.

[9] Q. Nie, The nonlinear evolution of vortex sheets withsurface tension in axi-symmetric flows, J. Comput. Phys., 174 (2001), 438–459.

[10] Q. Nie and F. Tian, Singularities in hele-shaw flows, SIAM J. Appl. Math., 58(1) (1998), 34–54.

[11] Q. Nie, Y. Zhang and R. Zhao, Efficient semi-implicit schemes for stiff systems, J. Comput. Phys., 214 (2006), 521–537.

[12] Y. Saad and M. H. Schultz, GMRES: A generalized minimal residual algorithm for nonsymmetric linear systems, SIAM J. Sci. Stat. Comput., 7 (1986), 856–869.

[13] I. Schmidt and D. Gross, The equilibrium shape of an elastically inhomogeneous inclusion, J. Mech. Phys. Solids, 45 (1997), 1521–1549.
[14] B. J. Spencer and D. I. Meiron, Nonlinear evolution of the stress-driven morphological instability in a 2-dimensional semiinfinite solid, Acta Metall. Mater., 42 (1994), 3629–3641.
[15] T. Hou, J. Lowengrub and M. Shelley, Removing the stiffness from interfacial flows with surface tension, J. Comput. Phys., 114 (1994), 312–338.
[16] W. H. Yang and D. J. Srolovitz, Crack-like surface instabilities in stressed solids, Phys. Rev. Lett., 71 (1993), 1593–1596.